

Mapping electron dynamics in highly transient EUV photon-induced plasmas

Citation for published version (APA):

Beckers, J., van de Wetering, F. M. J. H., Platier, B., van Nindhuijs, M. A. W., Brussaard, G. J. H., Banine, V. Y., & Luiten, O. J. (2019). Mapping electron dynamics in highly transient EUV photon-induced plasmas: a novel diagnostic approach using multi-mode microwave cavity resonance spectroscopy. *Journal of Physics D: Applied Physics*, 52(3), [034004]. <https://doi.org/10.1088/1361-6463/aaeb17>

Document license:
TAVERNE

DOI:
[10.1088/1361-6463/aaeb17](https://doi.org/10.1088/1361-6463/aaeb17)

Document status and date:
Published: 16/01/2019

Document Version:
Publisher's PDF, also known as Version of Record (includes final page, issue and volume numbers)

Please check the document version of this publication:

- A submitted manuscript is the version of the article upon submission and before peer-review. There can be important differences between the submitted version and the official published version of record. People interested in the research are advised to contact the author for the final version of the publication, or visit the DOI to the publisher's website.
- The final author version and the galley proof are versions of the publication after peer review.
- The final published version features the final layout of the paper including the volume, issue and page numbers.

[Link to publication](#)

General rights

Copyright and moral rights for the publications made accessible in the public portal are retained by the authors and/or other copyright owners and it is a condition of accessing publications that users recognise and abide by the legal requirements associated with these rights.

- Users may download and print one copy of any publication from the public portal for the purpose of private study or research.
- You may not further distribute the material or use it for any profit-making activity or commercial gain
- You may freely distribute the URL identifying the publication in the public portal.

If the publication is distributed under the terms of Article 25fa of the Dutch Copyright Act, indicated by the "Taverne" license above, please follow below link for the End User Agreement:

www.tue.nl/taverne

Take down policy

If you believe that this document breaches copyright please contact us at:

openaccess@tue.nl

providing details and we will investigate your claim.

PAPER

Mapping electron dynamics in highly transient EUV photon-induced plasmas: a novel diagnostic approach using multi-mode microwave cavity resonance spectroscopy

To cite this article: J Beckers *et al* 2019 *J. Phys. D: Appl. Phys.* **52** 034004

View the [article online](#) for updates and enhancements.



IOP | ebooks™

Bringing you innovative digital publishing with leading voices to create your essential collection of books in STEM research.

Start exploring the collection - download the first chapter of every title for free.

Mapping electron dynamics in highly transient EUV photon-induced plasmas: a novel diagnostic approach using multi-mode microwave cavity resonance spectroscopy

J Beckers¹ , F M J H van de Wetering¹, B Platier¹, M A W van Ninhuijs¹, G J H Brussaard², V Y Banine^{1,2} and O J Luiten¹

¹ Department of Applied Physics, Eindhoven University of Technology, PO Box 513, 5600MB Eindhoven, The Netherlands

² ASML, The Netherlands, PO Box 324, 5500AH Veldhoven, The Netherlands

E-mail: j.beckers@tue.nl

Received 30 July 2018, revised 12 October 2018

Accepted for publication 24 October 2018

Published 12 November 2018



Abstract

A new diagnostic approach using multi-mode microwave cavity resonance spectroscopy (MCRS) is introduced. This can be used to determine electron dynamics non-invasively in an absolute sense, as a function of time and spatially resolved. Using this approach, we have for the first time fully mapped electron dynamics specifically during the creation and decay of a highly transient pulsed plasma induced by irradiating a background gas with extreme ultraviolet (EUV) photons. In cylindrical geometry, electron densities as low as 10^{12} m^{-3} could be detected with a spatial resolution of (sub)100 μm and a temporal resolution of (sub)100 ns. Our experiments clearly show production of electrons even after the in-band EUV irradiation fades out. This phenomenon can be explained by both photoionization by out-of-band EUV radiation emitted by the EUV source later in time and delayed electron impact ionization by electrons initially created by in-band EUV photoionization. From the analysis, the absolute width of the electron cloud in the probing volume could also be retrieved temporally resolved. This data clearly indicates cooling of electrons. From an application perspective, it is demonstrated that the method can be used as a non-invasive and in-line monitor for ionizing radiation in terms of beam power, profile and pointing stability.

Keywords: microwave CAVITY resonance spectroscopy, photon induced plasma, EUV induced plasma, multi-mode MCRS, MCRS, electron density

(Some figures may appear in colour only in the online journal)

1. Introduction

The most essential step in the production of semiconductor circuits is photolithography. This multi-billion-dollar industry consistently adheres to Moore's law in printing an increasing number of transistors on a single chip. The smallest possible feature to be printed is dictated by the numerical aperture

(NA) of the system and the wavelength of the light used [1]. By scaling both, in recent decades scientists and technologists have successfully reached multiple industry-driven milestones. These include the introduction of immersion photolithography (increasing the NA of the system) and shortening the wavelength used. By far the most challenging step in this industry, however, is only now being taken: the introduction of extreme

ultraviolet (EUV) lithography [2] at a wavelength of 13.5 nm. Besides the extreme conditions needed to generate EUV photons, the full system requires a working pressure which is as low as possible in order to minimize photon absorption by background gas. Although the background conditions correspond to ultra-high vacuum, the system still requires a controlled amount of gas to be permanently present.

Inevitable when sending pulsed bunches of highly energetic (92 eV) photons through a gas—as low as its pressure might be—is the creation of an exotic type of plasma. This peculiar phenomenon is called EUV photon-induced plasma [3]. Not only is this kind of plasma highly transient in time, but the electron energy distribution is initially far from Maxwellian, with energies sufficiently high to produce even more plasma by means of electron impact ionization. Despite its relevance in outer space, research on the physical properties of EUV photon-induced plasmas has been scarce in literature. With the introduction of EUV lithography, however, several groups worldwide have now picked up this research topic. The reason for the industrial interest is that these plasmas will inevitably impact the operation of lithography tools in terms, for instance, of cleaning and the lifetime of delicate optical and other components [4–11].

EUV photon-induced plasmas have been modelled numerically by, for example, Abrikosov *et al* [12] and Astakhov *et al* [13]. From an experimental point of view, literature is scarcer, mainly because of the limited availability of the few and very expensive EUV-producing light sources. Experimental characterizations of EUV photon-induced plasma include monitoring the temporal evolution of the electron density [14–19] and studying the impact of ion fluxes on surfaces [20, 21].

In particular, studying the dynamics of the cloud of free electrons generates possibilities to reveal fundamental processes regarding plasma creation, plasma expansion, thermalization of the plasma and the dynamic formation of space charge regions, including their governing electric fields. Up until now, this electron density evolution has only been studied successfully using a non-invasive diagnostic called microwave cavity resonance spectroscopy (MCRS). Other traditional electron diagnostics such as Thomson scattering and the utilization of electric probes have appeared non-feasible under these conditions. For instance, the density of free electrons is far too low for Thomson scattering to deliver a sufficient signal [22], while van de Velden *et al* [23] showed back in 2008 that the use of electric probes was problematic for diagnosing photon-induced plasmas. Although absolute values for the density of free electrons could be retrieved from MCRS measurements [14–19], results have always been averaged over the full experiment volume and not corrected for the local electric field value of the resonant mode used. Hence, spatial information could not be retrieved using traditional MCRS. Only one experimental paper exists [16] in which the authors determine full-width-at-half-maximum (FWHM) values of spatial electron distribution functions by taking into account two resonant modes. Although a part of the electron dynamics could be described by these experiments, the results were not quantitative and not corrected

for the electric-field component of the microwave resonant modes used.

The novelty of this article is threefold.

- A novel diagnostic approach is developed and introduced, making traditional MCRS spatially resolved and electric-field corrected for the first time since its introduction in the 1950s [24].
- The electron dynamics in a highly transient plasma such as an EUV photon-induced plasma are both spatially mapped and temporally resolved, revealing new insights into plasma dynamics.
- From an application point of view, it is demonstrated how multi-mode MCRS can be applied as a beam power, profile and pointing stability monitor.

2. Method

2.1. MCRS principle

From a historical perspective, MCRS is based on a series of publications from the 1950s [24–26]. The last of these, in particular, proposes the use of interaction between electromagnetic fields in the microwave frequency regime and plasmas to probe the density of free electrons. Ever since, MCRS has been further developed and used to investigate the properties of many types of plasma. For instance, to measure the density of electrons in low-pressure radiofrequency-driven gas discharges [27]. In concert with laser-induced photodetachment, MCRS has even appeared to be an advantageous diagnostic to measure the density of negative ions in, for instance, etching plasmas [28–30] and powder-forming plasmas [31–34]. Since 2015, MCRS has been used to study the highly transient phenomena in plasmas generated by the irradiation of gas by ionizing (EUV) photons [13–15, 17–19, 35]. Full theoretical considerations regarding the MCRS technique have been described extensively in literature [27]. In this section, the working principle of this diagnostic is explained by mentioning only its key aspects. Readers are referred to the aforementioned literature for more details and mathematical background.

The essence of MCRS is that the plasma under investigation is produced inside a cylindrical pillbox cavity. The geometry of this cavity is designed such that resonant modes can be excited at resonance frequencies in the microwave (MW) range (a few GHz). The exact frequency at which a certain resonant mode exists is defined mainly by the geometrical configuration of the cavity (which is fixed during experiments) and the permittivity $\epsilon = \epsilon_0\epsilon_r$ of the medium inside the cavity. For a fixed cavity, multiple resonant modes may exist over a certain frequency range. Two types of resonant modes are usually recognized: transverse electric, TE_{mnp} , and transverse magnetic, TM_{mnp} , with $m = 0, 1, 2, \dots$ (for TE: $m = 1, 2, 3, \dots$), $n = 1, 2, 3, \dots$ and $p = 0, 1, 2, \dots$.

The quantitative diagnostic approach of MCRS is based on the fact that the presence of free charge carriers (in this case plasma) directly gives rise to a finite increase in ϵ_r as [30]

$$\epsilon_r = 1 - \frac{\omega_{pe}^2}{\omega^2 + \nu^2} + i \frac{1}{Q_0} \approx 1 - \frac{\omega_{pe}^2}{\omega^2} + i \frac{1}{Q_0}. \quad (1)$$

In this equation, the term $i \frac{1}{Q_0}$ (with i the imaginary unit) accounts for losses due to non-idealities of (or in) the cavity while the collision frequency ν between electrons and other particles—which is usually considered as a loss term as well—is negligible in our case due to the low gas and electron densities. As will be described later in this article, the quality factor ‘ Q ’ is a measure of the rate at which a cavity can be loaded or reloaded with microwave energy and therefore determines the response time of the diagnostic under discussion. As can be seen in equation (1), ϵ_r depends on the angular frequency ω of the microwave field used and the electron plasma frequency ω_{pe} given by:

$$\omega_{pe} = \sqrt{\frac{n_e e^2}{m_e \epsilon_0}}, \quad (2)$$

where m_e and e are the mass of an electron and the elementary charge respectively, and ϵ_0 the permittivity of vacuum. The diagnostic force becomes immediately clear when we realize that the electron plasma frequency—and therefore ϵ_r as well—is directly affected by the electron density n_e .

Since the diagnostic is operated in the microwave regime, the inertia of ions and heavier charge carriers (e.g. nanometre and micrometre-sized particles) is too large to allow these particles to follow the electric field oscillations. Unlike ions, electrons are sufficiently mobile to follow the microwave fields applied and therefore to determine the permittivity of the plasma.

Overall, compared with the situation in vacuum, the presence of free electrons inside the cavity affects ϵ , while in turn ϵ affects the resonance frequency $f_0 = \omega_0/2\pi$ of the resonant mode used. In the diagnostic presented here, a lossless and isotropic cavity medium with permittivity $\epsilon(\mathbf{x})$ and permeability $\mu(\mathbf{x})$ is assumed. This means that the electric field \mathbf{E} and electric displacement field \mathbf{D} of a resonant mode are related by $\mathbf{D} = \epsilon\mathbf{E}$. For the magnetic fields, a similar relationship holds: $\mathbf{B} = \mu\mathbf{H}$. The current application focuses on unmagnetized low-pressure and non-thermal plasmas, for which it is common to assume $\mu(\mathbf{x}) = \mu_0$ and that the ions are immobile and cold. It can be derived from [36] that the electric-field-averaged electron density \bar{n}_e inside a cavity relates to the resonance frequencies f_0 and f of a specific resonant mode in an empty cavity and in a cavity partly or completely filled with free electrons, i.e. plasma, respectively as:

$$\bar{n}_e = \frac{8\pi^2 m_e \epsilon_0 f^2 \Delta f}{e^2 f_0}, \quad (3)$$

with $\Delta f \stackrel{\text{def}}{=} f - f_0 > 0$ the resonant frequency shift due to the presence of plasma. Note that \bar{n}_e is an electric-field-averaged electron density taking into account both the spatial distribution of the free electrons over the cavity volume $n_e(\mathbf{x})$ and the local value of the electric-field component $\mathbf{E}(\mathbf{x})$ of the MW resonant mode.

$$\bar{n}_e \stackrel{\text{def}}{=} \frac{\int \int \int_{\text{cav}} n_e(\mathbf{x}) |\mathbf{E}(\mathbf{x})|^2 d^3x}{\int \int \int_{\text{cav}} |\mathbf{E}(\mathbf{x})|^2 d^3x}. \quad (4)$$

This means that, depending on the resonant mode used, electrons at different positions in the cavity are probed to a different extent. Hence, MCRS yields electron densities which are inherently cavity-averaged and electric-field weighted.

Until now, this has always been experienced as a disadvantage of the MCRS technique. However, the analysis and comparison of multiple modes can serve to resolve the electron density distribution spatially. Successful application of this method is demonstrated in the current article.

2.2. Multi-mode MCRS

As already mentioned in the previous section, the extent to which free electrons are probed by the MCRS diagnostic scales directly with the local value of $\mathbf{E}(\mathbf{x})$ of the specific resonant mode. Hence, the resonance frequency shift Δf induced by the local presence of electrons is different for each resonant mode. Six examples of computed $\mathbf{E}(\mathbf{x})$ components of different resonant modes in an ideal cylindrical cavity are given in figure 1.

Taking into account equation (4), it can be reasoned that electrons present on the axis of this cavity are probed with a high weighting factor (large Δf) by the resonant TM_{010} and TM_{020} modes because $\mathbf{E}(\mathbf{x})$ is at its maximum on the axis. At the same time, the same electrons are hardly detected by the other modes shown in figure 1 because these show $\mathbf{E}(\mathbf{x}) = 0$ on the axis. It is precisely this difference in the spatial sensitivity of the different resonant modes to the presence of free electrons which is used to make multi-mode MCRS spatially resolved. The procedure to achieve this is elaborated in the following section.

2.2.1. Reconstruction of electron density distribution profile.

To obtain spatially resolved electron density profiles, MCRS is applied in N resonant modes and for each time step and resonant mode the shift in resonance frequency $\Delta f_1; \Delta f_2; \dots; \Delta f_N$ caused by the presence of free electrons is measured. From these values, the cavity-averaged and electric-field-weighted electron densities $\bar{n}_{e,1}; \bar{n}_{e,2}; \dots; \bar{n}_{e,N}$ can be calculated using equation (3). For each (i,j) combination of resonant modes ($j > i$), the ratio between the respective $\bar{n}_{e,i}$ and $\bar{n}_{e,j}$ values is determined as $r_{ij}^{\text{meas}} = \bar{n}_{e,i}/\bar{n}_{e,j}$. In parallel, from a theoretical perspective, the similar ratios r_{ij}^{theory} are determined by assuming a certain spatial n_e profile shape. Corresponding with measurements of the intensity profile of the initial irradiation profile (see figure 12(b)), a Gaussian profile has been considered here. However, it should be noted that every other possible profile shape (e.g. Bessel-like) might and can be used if the actual plasma physical situation demands so.

The reconstructed profile corresponds with the smallest root-mean-square error ξ_k between r_{ij}^{meas} and r_{ij}^{theory} ,

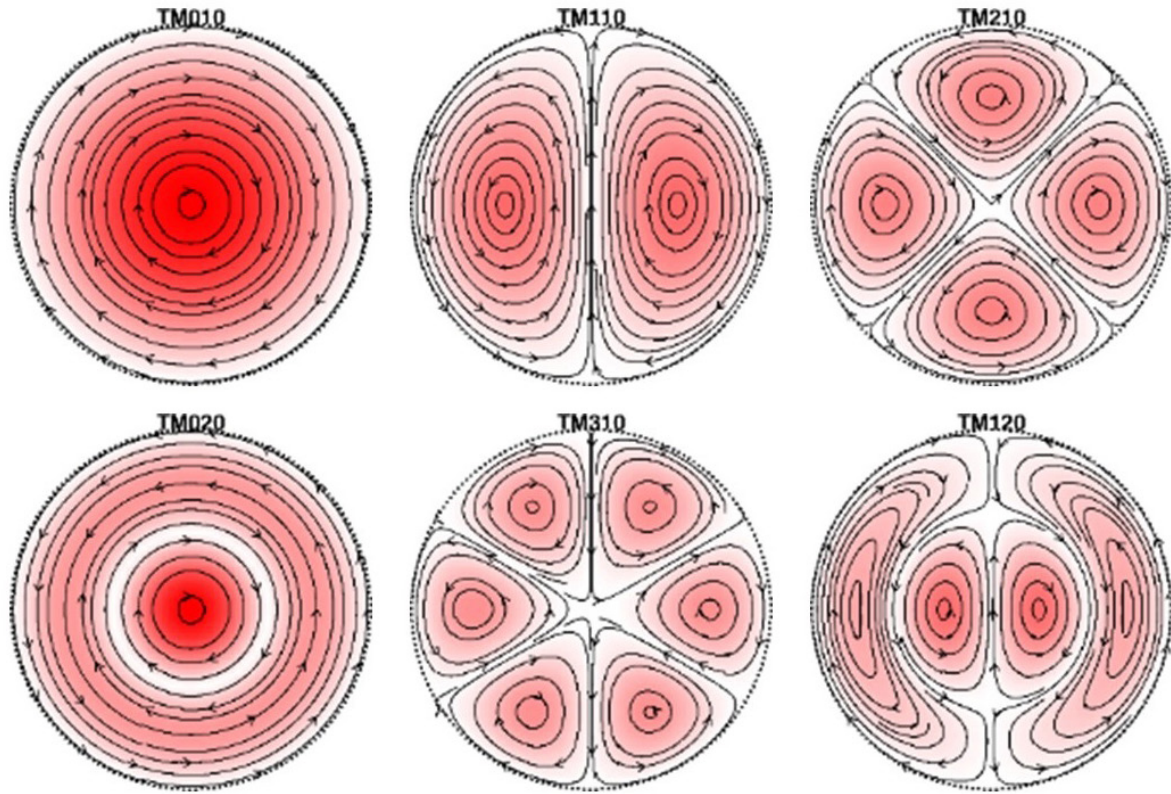


Figure 1. Analytically computed electric-field distributions (red is a high electric field magnitude, white a low electric field magnitude) and magnetic field lines (arrows) for several possible resonant modes in an ideal cylindrical cavity (dashed). The axis of symmetry (z) is pointing away from the paper.

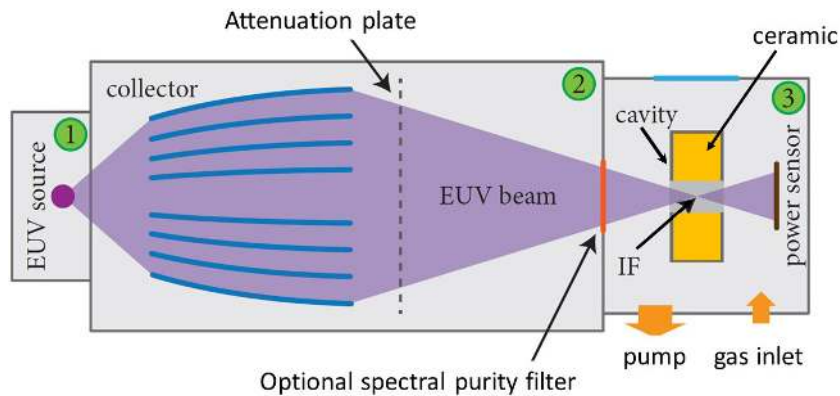


Figure 2. Schematic representation of the experimental setup used, with (1) the source chamber housing the EUV source, (2) the collector chamber housing the collector, an attenuation plate and, optionally, a spectral purity filter and (3) the measurement chamber housing the resonant cavity. The collector focuses the EUV beam in the intermediate focus (IF). Adapted with permission from [37]. Copyright © 2015 R. M. van der Horst.

$$\xi_k = \sum_{j>i}^N \left(\frac{r_{ij}^{\text{theory}} - r_{ij}^{\text{meas}}}{r_{ij}^{\text{theory}}} \right)^2, \quad (5)$$

which is brute-force calculated over a range of centre positions (x_0, y_0) and widths σ of the 2D Gaussian electron density profiles,

$$n_e(x, y) = n_e^{\text{max}} \exp \left(-\frac{(x - x_0)^2 + (y - y_0)^2}{2\sigma^2} \right). \quad (6)$$

Note that, since the modes used in this work all have field components which are axially independent (despite small deviations close to the entrance and exit holes of the cavity), and also the xy intensity profiles of the beam used does not change along the z -direction inside the cavity, $n_e(x, y)$ is independent of z .

This reconstruction procedure can be run for each time step for which experimental data for $\Delta f_1; \Delta f_2; \dots; \Delta f_N$ is available. Therefore, the output of the reconstruction method we have developed in-house is the centre position $(x_0(t), y_0(t))$ of the maximum of the electron density profile and its width

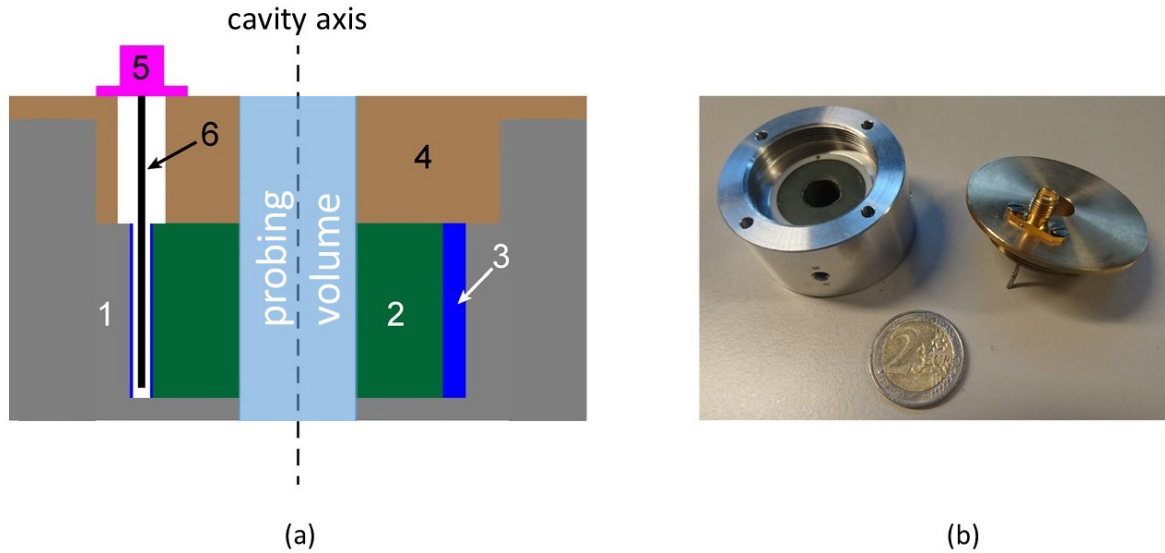


Figure 3. Schematic diagram (a) and photograph (b) of the basic cavity design with (1) aluminium cavity base, (2) ceramic with relative permittivity of approximately 37 in the MW regime, (3) Teflon centring ring with a slot in the axial direction for the MW antenna, (4) brass cavity enclosure, (5) SMA connector, and (6) straight MW antenna. The cavity base contains slots for housing cartridge heaters and Pt1000 temperature sensors.

$\sigma(t)$ with—in the case of reproducible plasma events—a temporal resolution limited by the Q of the cavity and the resonant mode used. The spatial resolution (of the reconstruction algorithm) of the centre position is $100\ \mu\text{m}$ and that for the width is $10\ \mu\text{m}$. Volume integrals are calculated numerically, with electric fields and electron densities averaged along the axis of the cavity (z -axis) since we are only interested in and calculate 2D $n_e(x, y)$ profiles (equation (6)),

$$\int \int \int_{\text{cav}} n_e(\mathbf{x}) |\mathbf{E}(\mathbf{x})|^2 d^3\mathbf{x} \rightarrow \int \int_{\text{cav}} n_e(x, y) |\mathbf{E}(x, y)|^2 dx dy \approx \delta^2 \sum_{i=1}^{N_{xy}} n_e(x_i, y_i) |\mathbf{E}(x_i, y_i)|^2, \quad (7)$$

$$\int \int \int_{\text{cav}} |\mathbf{E}(\mathbf{x})|^2 d^3\mathbf{x} \rightarrow \int \int_{\text{cav}} |\mathbf{E}(x, y)|^2 dx dy \approx \delta^2 \sum_{i=1}^{N_{xy}} |\mathbf{E}(x_i, y_i)|^2, \quad (8)$$

where N_{xy} is the number of grid points in the xy -plane and $\delta = 100\ \mu\text{m}$ the constant spacing of the grid points in both the x - and y -direction; and

$$\mathbf{E}(x, y) \stackrel{\text{def}}{=} \frac{1}{N_z} \sum_{i=1}^{N_z} \mathbf{E}(x, y, z_i), \quad (9)$$

where N_z is the number of grid points in the z -direction.

For $\mathbf{E}(x, y, z)$, fields simulated with CST Microwave Studio (see appendix A for detailed information and the computed E-field profiles) have been used as input. Furthermore, it is assumed that the electron density is zero outside the probing volume (see figure 3).

2.2.2. Restoring absolute values. Since the reconstruction algorithm optimizes x_0 , y_0 and σ for the smallest value of ξ_k , the maximum value of the profile n_e^{max} is lost and has to be

determined during post-processing. To this end, equation (4) is solved for n_e^{max} but now using the reconstructed 2D n_e profile (with numerical approximations similar to those above),

$$n_{e,i}^{\text{max}} = \bar{n}_{e,i} \frac{\int \int_{\text{cav}} |\mathbf{E}_i(x, y)|^2 dx dy}{\int \int_{\text{cav}} \exp\left(-\frac{(x-x_0)^2 + (y-y_0)^2}{2\sigma^2}\right) |\mathbf{E}_i(x, y)|^2 dx dy}, \quad (10)$$

where i signifies a certain resonant mode. Irrespective of the combination of modes used for the reconstruction, n_e^{max} is calculated for all N modes that show good agreement between experimentally determined E-field profiles using the bead-scanning method (see appendix B) and the ones simulated using CST Microwave Studio (see appendix A). Subsequently, the mean value $\langle n_e^{\text{max}} \rangle$ and standard error s associated with it is calculated as

$$\langle n_e^{\text{max}} \rangle = \frac{1}{N} \sum_{i=1}^N n_{e,i}^{\text{max}}, \quad (11)$$

$$s = \frac{\sigma_{\text{sample}}}{\sqrt{N}}, \quad (12)$$

where σ_{sample} is the uncertainty on each value. The 95% confidence interval of $\langle n_e^{\text{max}} \rangle$ is given by roughly $\pm 2s$.

3. Experiment

3.1. Experimental configuration

The experimental configuration used is depicted schematically in figure 2. Mechanically, broadly speaking the setup consists of three chambers: the source chamber, the collector chamber and the measurement chamber. The radiation source—housed in the source chamber—is a discharge-produced pinch plasma in xenon gas, producing pulsed radiation

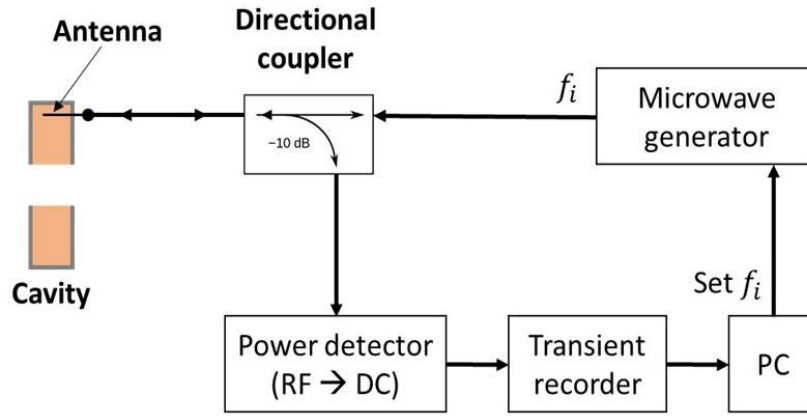


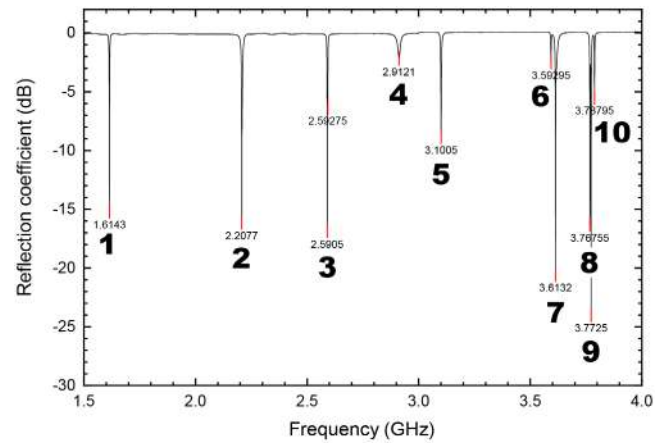
Figure 4. Schematic diagram of the data-acquisition system.

including contributions with wavelengths in the EUV range. All the features of this source have been described extensively in [14, 37]. In the configuration used, the pulsed radiation produced by the EUV source has a repetition rate of 500 Hz, a pulse duration of roughly 100 ns and a pulse energy of 125 μJ in the 10–20 nm wavelength range.

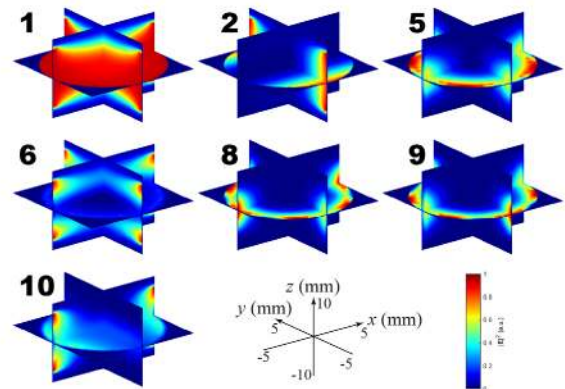
The collector chamber (1.5 m in length and 1 m in diameter) houses the collector, which is a set of grazing-incidence multilayer mirrors in ‘Wolter’ configuration (aligned in an ‘onion-like’ structure) as described in, for instance, [38]. This collector focuses the light emitted by the EUV source in the intermediate focus IF in the measurement chamber. In the IF, the beam waist is approximately 4 mm and the beam has a divergence of 10° [37]. Although this setup has the option to install a spectral purity filter between the collector and the measurement chamber, none was used during the experiments presented here. The measurement chamber houses the microwave resonant cavity through which EUV photons can be directed without releasing any electrons from the walls by photoelectric effects. The spectrally integrated EUV power is monitored by a thermal EUV power sensor with an experimental error of 6% [37].

3.2. Cavity design

A schematic diagram and a photograph of the cylindrical cavity developed for this work are provided in figure 3. The base of the cavity is an aluminium body with a screw-on brass lid. Fully mounted, the inner diameter of the cavity is 29 mm and its inner height is 15 mm. Two concentric holes in the brass lid and in the base of the cavity, aligned at the cavity axis, allow irradiation of the gas inside with EUV photons without creating photoelectrons from the cavity walls. These photon entrance and exit holes both have a diameter of 10 mm. Based on the work of Lassise *et al* [39, 40] on making small and power-efficient cavities, the cavity is partly filled with a ZrTiO_4 ceramic between a radius of 5 mm and 12.5 mm. This ceramic from T-CERAM (‘E-37’) was chosen for its low loss term $\tan \delta = 2 \times 10^{-4}$ and its high $\epsilon_r = 37$ (at 10 GHz) [40]. Whilst using a material with a low loss term is largely relevant for these applications, a high ϵ_r could be advantageous for two reasons. First, the high permittivity makes the cavity larger



(a)



(b)

Figure 5. (a) Response of the developed microwave resonant cavity as a function of excitation frequency in the range 1.5–4.0 GHz; (b) simulated electric-field profiles in the probing volume of the cavity used for further multi-mode MCRS analysis.

in a virtual sense, meaning that the resonant modes used can be excited at lower resonant frequencies. This in turn means that the holes in the lid and base can be drilled larger without causing significant ‘leakage’ of microwave radiation from the cavity. Second, the mode shows field concentration around the axis of the cavity while the ratio between the volume with

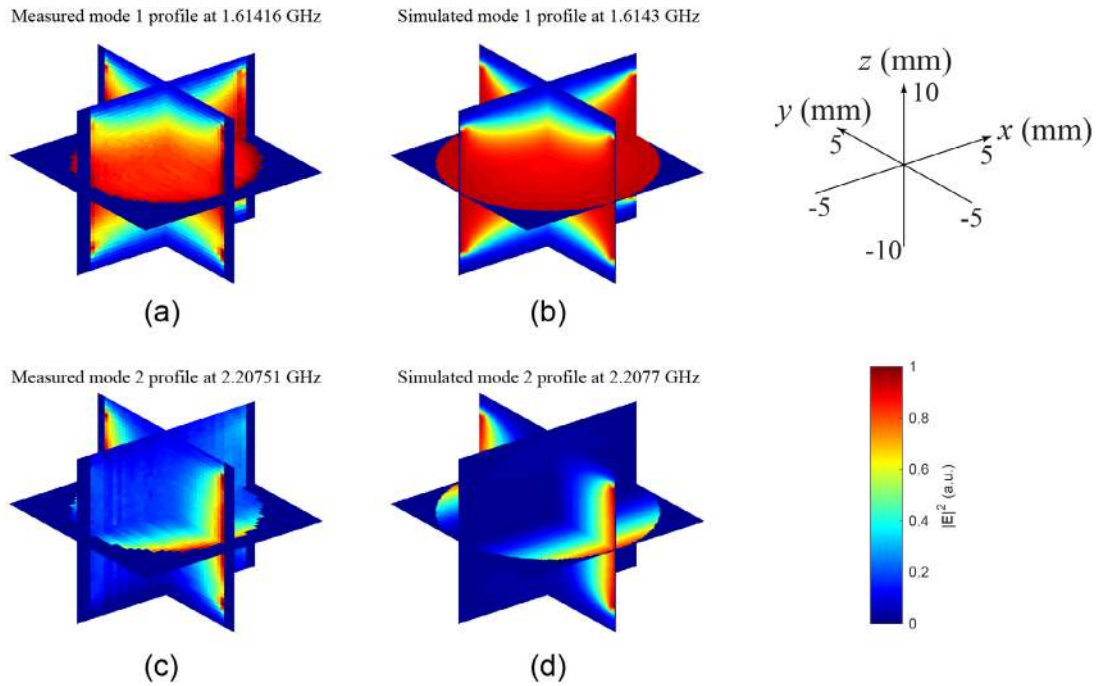


Figure 6. Electric-field profiles obtained experimentally using the bead-scanning method (a), (c) and simulated using the CST Microwave Studio package (b) and (d), for modes 1 (a), (b) and 2 (c), (d). Results from the bead-scanning method correspond well with the simulations.

which plasma is created by the EUV irradiation and the total cavity volume is also much larger. This combination results in a significant improvement overall in the signal-to-noise ratio of the diagnostic. It is impossible to neatly drill a small hole in the ceramic, so it was decided instead to position the (straight) antenna used to excite the MW modes outside the ceramic material, very close to the inner cavity wall. To keep the ceramic in place, a Teflon centring ring fills the gap between the cavity wall and ceramic (between a radius of 12.5 mm and 14.5 mm). The antenna used, which slides into the slot in the Teflon ring, is a straight and fixed piece of copper wire (diameter 1 mm, length approximately 20 mm) connected to the MW source by a fixed SMA feedthrough. To be able to heat the cavity to a set temperature (and keep it stable there), the aluminium housing includes four slots housing cartridge heaters and one slot that can house a Pt1000 temperature sensor. It also has four M4 holes in the outer side wall (at half height), to be able to fix it in the setup.

3.3. Data-acquisition hardware

A schematic diagram of the acquisition system is provided in figure 4. Unlike past MCRS measurements by the EPG research group, which used two loop antennas as a sender-receiver pair for transmission measurements, ours are performed in reflection mode using a single straight antenna. A microwave generator (Stanford Research Systems SG386) produces a sinusoidal microwave signal at 16 dBm power and at a frequency set by the PC. This output is connected to the output port of a directional coupler (Mini-Circuits ZHDC-10-63-S+) and in principle passes unhindered to its input port, which is connected to the antenna inside the cavity. In this

Table 1. Resonance frequency f_0 and FWHM Γ , together with the resulting Q and cavity response time, for each of the resonant modes of the cavity developed in this work.

	f_0 (GHz)	Γ (MHz)	Q	τ (ns)
Mode 1	1.610	3.12	517	102
Mode 2	2.209	4.73	467	67
Mode 5	3.104	4.43	701	72
Mode 6	3.594	2.60	1382	122
Mode 8	3.771	2.83	1333	112
Mode 9	3.776	3.30	1144	96
Mode 10	3.788	2.19	1730	145

way, resonances can be excited in the cavity by applying the correct output frequency from the microwave generator. If the cavity is off resonance, power coupling to it is very inefficient and most of the power reaching the antenna reflects back to the microwave generator, where it is dissipated. Part of this signal (10%), however, is rerouted by the directional coupler to the measurement leg of the detection system, where it is first converted to DC by a logarithmic power detector (Hittite 602LP4E, 10 ns rise and fall time) and subsequently fed to a high-frequency (up to 250 MHz, but for the current measurements set to 50 MHz) transient recorder (Spectrum M3i.4121-exp) inside the same PC. The transient recorder continuously samples its input port and stores the data in its internal memory. Only upon an external TTL trigger, for which the trigger signal produced by the EUV source related to the discharge between the electrodes is used, is data made available to the user for subsequent analysis. This arrangement allows us to analyse part of the signal before the actual trigger occurs. If the cavity is at resonance, hardly any signal reflects back (most of the energy is dissipated in the

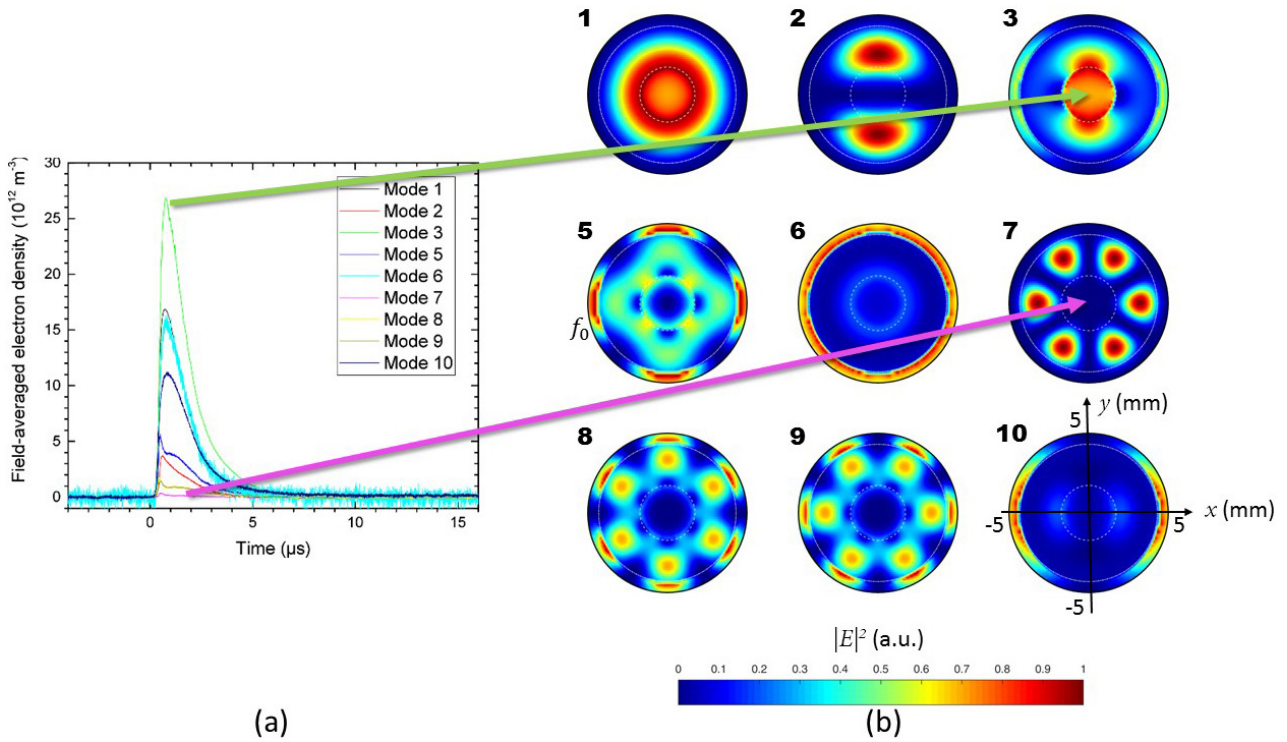


Figure 7. (a) Cavity-averaged values of \bar{n}_e as a function of time before and after the gas was irradiated with a pulse of EUV radiation (at $t = 0$) obtained from different resonant modes and (b) simulated electric-field profiles through the whole cavity volume (including the ceramic and Teflon) for each of these modes. Background gas pressure was 10^{-4} mbar. The EUV beam was aligned axially at the centre of the cavity.

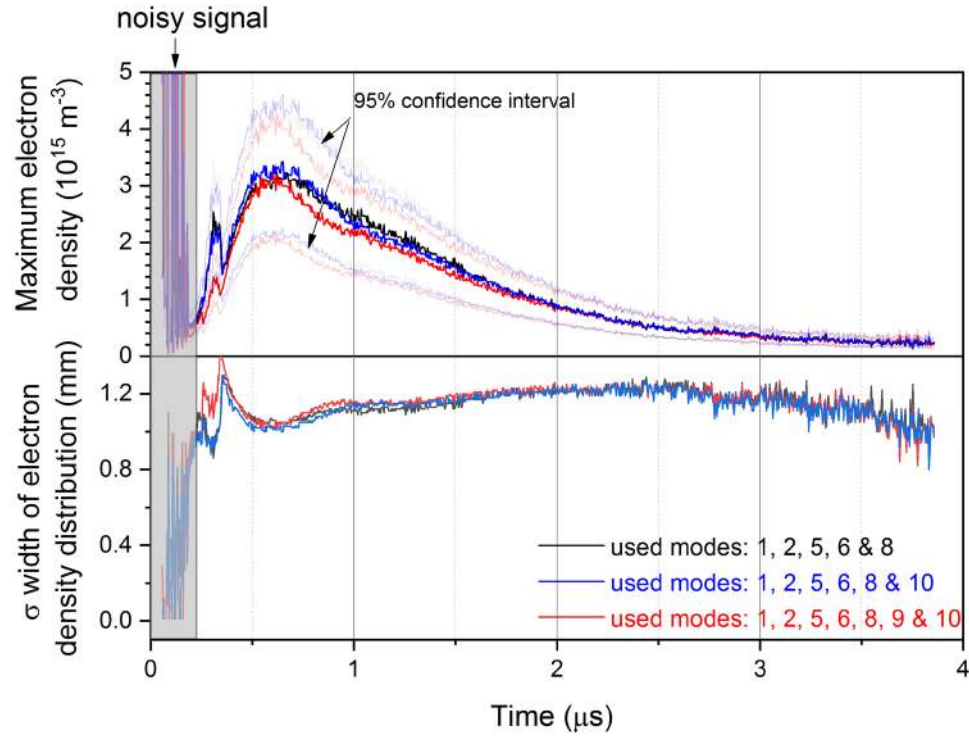


Figure 8. Top: maximum electron density (n_e^{max}) as a function of time after gas irradiation combining respectively five, six and seven different modes (see inset for the specific modes used). The greyed-out curves indicate the upper and lower limits of the corresponding 95% confidence interval. Bottom: temporal evolution of the radial width σ of the electron density distribution retrieved from the same data.

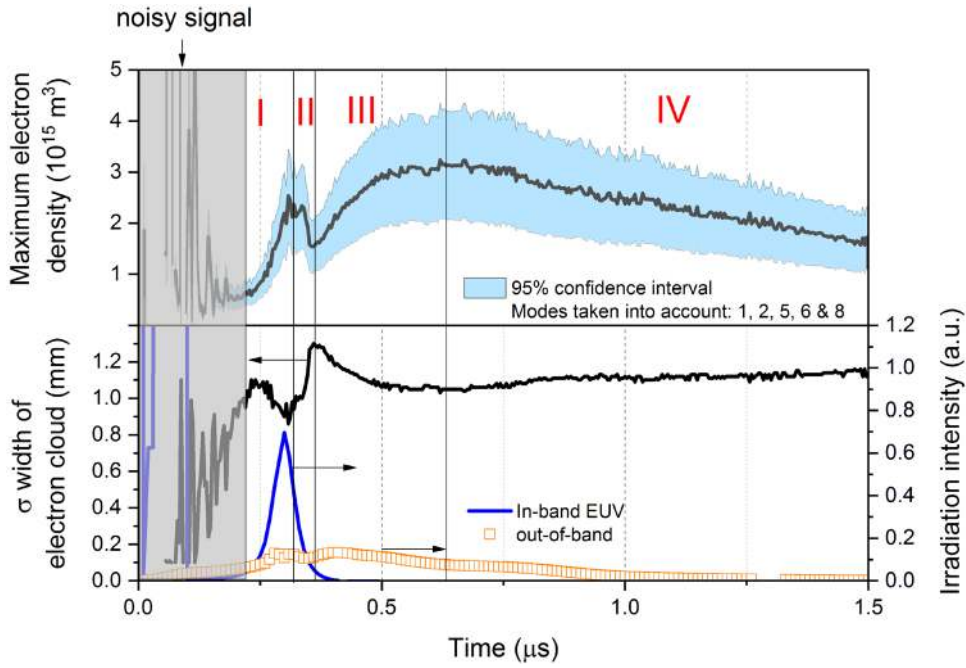


Figure 9. Top: maximum electron density $\langle n_e^{\max} \rangle$ as a function of time using modes 1, 2, 5, 6 and 8, together with the corresponding 95% confidence interval. Bottom: temporal evolution of the radial width σ of the electron density distribution retrieved from the same data together with independently measured in-band EUV radiation and out-of-band radiation from the same xenon-pinch discharge source [37]. The time axes have been aligned with one another.

electromagnetic field inside the cavity) and that probed by the transient recorder is low. Data analysis is similar to that discussed in previous work [33, 37, 41, 42], differing only in the ‘direction’ of the resonance peaks (maxima versus minima, see figure 5).

During the measurements presented in this paper, the microwave source was set to a certain frequency and kept at this frequency during the entire duration of the EUV pulse and the measurement time after this pulse. Just before the gas in the cavity is exposed to the next EUV pulse, the microwave source is set to the next value. To obtain sufficient accuracy, a resonant peak is probed by measurements at 25 different frequencies located in the frequency domain closely around the resonant frequency.

3.4. Calibration and characterization of the cavity

In order to translate the measurements taken into quantitative results, (i) each resonant mode has to be identified and (ii) the electric-field profile of each resonant mode used must be spatially resolved in a known manner. To this end, the electric-field profiles are obtained in two ways: numerically, using the commercially available Microwave Studio simulation package (see appendix A), and experimentally using the ‘bead-scanning’ method (see appendix B).

Figure 5(a) shows the cavity-response spectrum in the frequency range 1.5 to 4.0 GHz. In this spectrum, 10 resonant modes can be identified. But only those (modes 1, 2, 5, 6, 8, 9 and 10) for which the electric-field profiles obtained by the bead-scanning method and from CST Microwave Studio show reasonable agreement are taken into account for further multi-mode MCRS analysis. As an example, figure 6 shows the

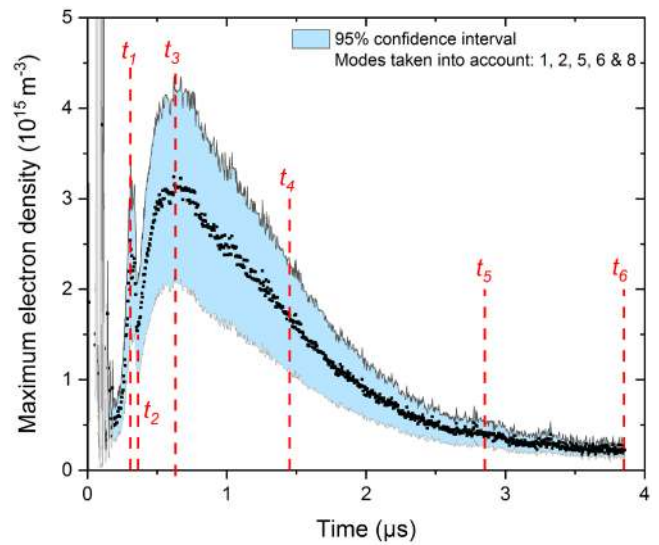


Figure 10. Maximum electron density $\langle n_e^{\max} \rangle$ as a function of time. The red dashed lines indicate the moments when spatially resolved electron density distributions have been reconstructed. These results are plotted in figure 11.

experimentally and numerically determined field profiles for the first two modes; results for the others used can be found and compared in figure C1 in appendix C.

Figure 5(b) shows those (simulated) electric-field profiles in the cavity probing volume to be used for further analysis.

In MCRS in general, the Q -factor (or ‘ Q ’) is a crucial parameter when it comes to limitations in terms of resolution in time and accuracy in \bar{n}_e determination. This factor is defined as the ratio between the energy stored in the cavity and the energy dissipated per cycle due to non-idealities. It can be

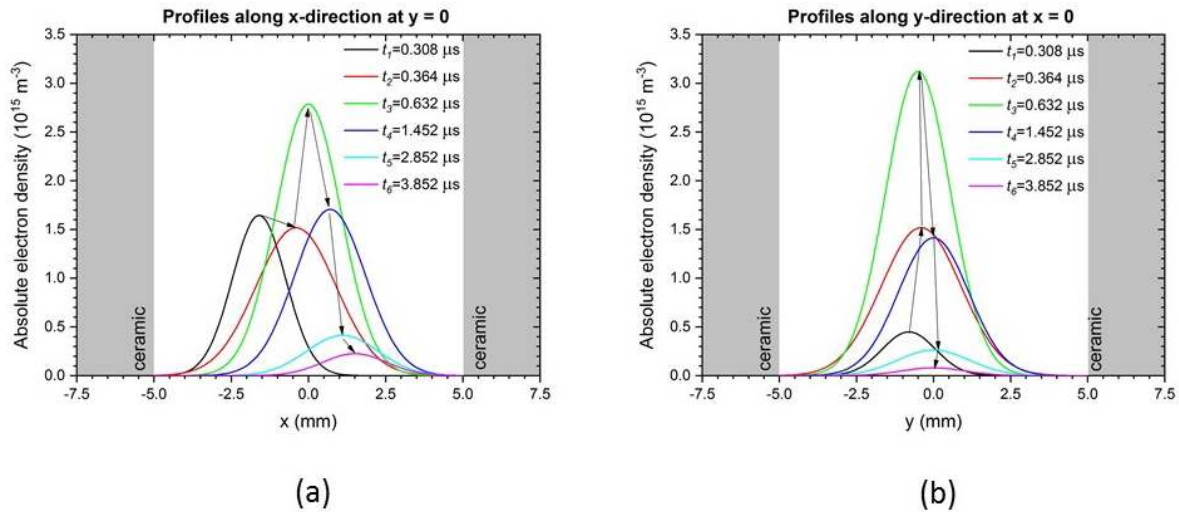


Figure 11. Absolutely calibrated and spatially resolved electron density profiles for six different moments in time along the cavity x -axis (a) and y -axis (b).

deduced from the measured FWHM Γ and the frequency f at which this resonance curve shows its maximum

$$Q \stackrel{\text{def}}{=} \frac{f}{\Gamma}. \quad (13)$$

The higher the ‘level of perfectness’ or Q of a cavity, the more energy can be stored in it and the lower the energy-dissipation rate due to imperfections. This means that cavities with a high Q have a narrow resonance curve which results in accurate determination of \bar{n}_e . At the same time, a high Q results into a slow response by the cavity to changes in permittivity and hence in \bar{n}_e . The $1/e$ response time τ of the cavity relates to Q and resonance frequency of a specific resonant mode as:

$$\tau = \frac{Q}{\pi f}. \quad (14)$$

In practice, when designing a cavity one should tweak Q in order to find a suitable optimum between accuracy in \bar{n}_e determination and the time resolution of the diagnostics. The resonant modes of our cavity have Q ’s listed in table 1 together with the corresponding cavity response times, which are in the order of 100 ns.

The current diagnostic has a huge dynamic range but still is limited. For instance, the lower detection limit is noise-determined. The upper detection limit of MCRS is determined by the moment at which the perturbation theory of Maier and Slater [43] is no longer valid ($\epsilon_r \ll 1$). The lower detection limit has—up until now [14, 15, 18, 19]—been demonstrated to be in the order of 10^{13} m^{-3} , while in our work the sensitivity is improved by one order of magnitude. The upper detection limit is 10^{18} m^{-3} . Expected values of \bar{n}_e in the EUV-induced plasma under the current conditions are between the lower detection limit and 10^{16} m^{-3} . Hence, MCRS is a suitable diagnostic for studying this kind of plasma system.

4. Results and discussion

Multi-mode MCRS has been applied to a highly transient plasma induced by irradiation of a residual background gas

at 10^{-4} mbar with pulsed EUV radiation. The cavity geometry used is as introduced and discussed in 3.2. The results and discussion presented in this section are divided into three parts. Section 4.1 demonstrates the multi-mode MCRS method through the generation of absolutely calibrated electron densities from traditional MCRS measurements using different resonant modes. Section 4.2 uses these multi-mode MCRS measurements to reveal new physical insights into the dynamics of EUV-induced plasmas. For instance, unexpected phenomena such as additional electron production even after extinguishing of the main EUV pulse have been observed, an effect which can be explained by the presence of unfiltered radiation from the xenon-pinch-discharge EUV source and the governing interaction of this radiation with gas. Finally, section 4.3 demonstrates that (and how) multi-mode MCRS can be applied as a non-intrusive *in situ* beam power, profile and pointing stability monitor for ionizing radiation [44].

4.1. Multi-mode MCRS: from volume averaged to ‘real’ electron densities

The cavity-averaged and E-field-weighted density of free electrons \bar{n}_e obtained from traditional MCRS using different resonant modes is depicted on the left-hand side of figure 7 as a function of time before and after irradiation of the gas with a pulse of EUV photons. On the right-hand side are shown simulated electric-field profiles through the whole cavity volume (including the ceramic and Teflon) for each of these resonant modes. Note that modes 8 and 9 are basically identical, with the only dissimilarity being that their axes of symmetry are tilted slightly differently in the xy -plane. Note that in this case the cylindrical symmetry of the excited modes in the cavity is broken by the presence of the antenna. From these cavity-averaged results, two interesting features can already be identified. First, whereas van der Horst *et al* [17] found MCRS suitable for detecting \bar{n}_e down to 10^{13} m^{-3} , in our work better cavity design and fitting procedures have resulted in a lower detection limit improved by one order of magnitude (down to $\bar{n}_e \approx 10^{12} \text{ m}^{-3}$). This opens the door for the study of plasma

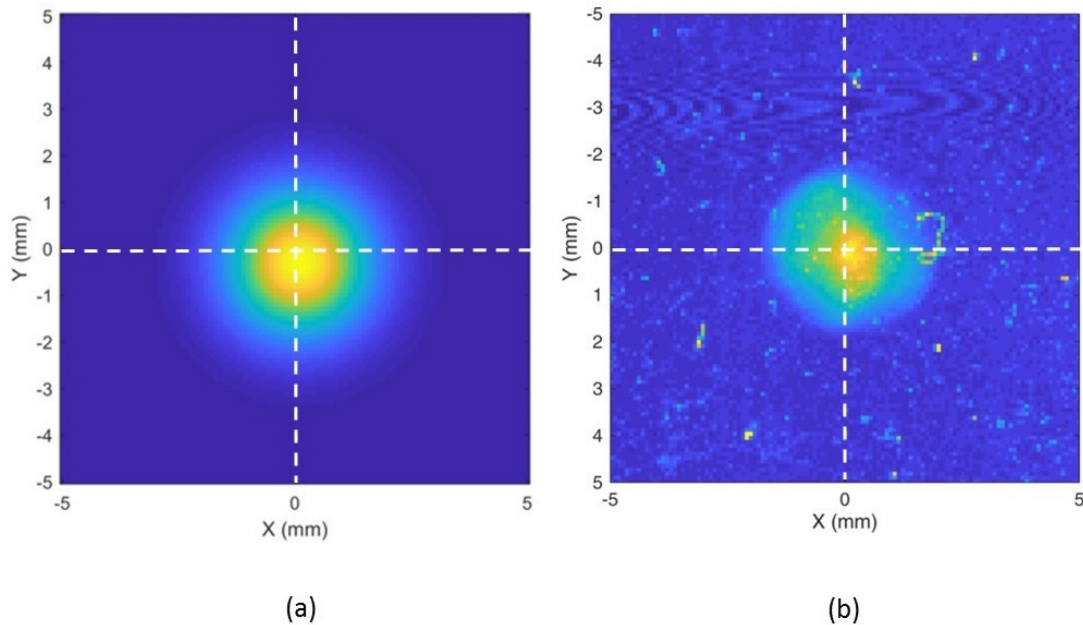


Figure 12. (a) Reconstructed n_e profile at the maximum intensity of in-band EUV emission and (b) an independent measurement of the beam-intensity profile at the position of the cavity. Reproduced with permission from [47].

dynamics at much lower gas pressures, as demonstrated in this article. Second, absolute values of \bar{n}_e and its development as a function of time appear to depend largely on the resonant mode used. This indicates that spatial information about the distribution of \bar{n}_e over the cavity volume is indeed hidden within the data. As already explained in section 2, time-resolved MCRS measurements of \bar{n}_e at multiple resonant modes form the basic ‘raw’ data for further analysis.

In the procedure we have developed, this ‘raw’ data is used to derive the absolutely calibrated maximum value of the electron density (n_e^{\max}), in a temporally resolved fashion. Note that—although only maximum values are presented in this section—our procedure is able to reconstruct absolutely calibrated and fully spatially resolved electron density profiles (as will be demonstrated in the next section). For reconstruction and absolute calibration, the field profiles of respectively five, six and seven different microwave resonant modes have been combined. For each set, figure 8 plots the results together with the upper and lower limit of the corresponding 95% confidence interval and the temporal evolution of the radial width σ of the calculated electron density distribution.

From this figure, it can be concluded that—especially during the first 220 ns of the profiles shown—the signals contain too much noise to deliver valuable information. This noise is caused by EMC from the EUV source just before it emits the main in-band EUV radiation and is more dominant in our measurements than in those in other literature [14] because no spectral purity filter (SPF) has been used here (SPF normally blocks part of the EMC from the source). Between 220 ns and 380 ns, the general trend for the different sets of resonant modes used appears to be the same but the absolute values are not consistent. The reason for this is that timescales for plasma dynamics in this range are of the same order as the response time τ of the cavity used (roughly

100 ns, see table 1). Since τ is different for different resonant modes, it is not surprising that the $\langle n_e^{\max} \rangle$ and σ curves diverge from one another when different sets of resonant modes are used to construct them. In this range, it is important to note that, although absolute values of the electron density and its spatial distribution width might not be very accurate, trends in temporal evolution can be made visible at sub-100 ns time-scales. The reason for this is that MCRS reacts to trends even when the specific resonant modes are not yet fully loaded. Beyond 380 ns, the same results are produced when taking into account different sets of resonant modes. This indicates the reliability—in terms not only of temporal evolution, but also of absolute values—of the multi-mode MCRS approach we have developed.

4.2. Multi-mode MCRS: mapping electron dynamics at low-pressure EUV photon-induced plasmas

A zoomed-in picture of the curves reconstructed using modes 1, 2, 5, 6 and 8 is presented in figure 9 with—for clarity—independently measured [37] (but synchronized in time with the other data) out-of-band and in-band EUV-radiation intensity delivered by the same EUV source at the same position in the cavity.

In order to discuss the plasma dynamics involved, the time evolution of the system has been divided in four different phases (denoted I–IV in figure 9). As already explained in the previous section, dynamic processes in phases III and IV are sufficiently slow, compared with the cavity response time τ , to deliver accurate and absolute results. Processes and time behaviour in phases I and II are of the same order as or faster than τ , meaning that although dynamics can be probed in relative sense using this method, absolute values may be less accurate.

As can be observed from figure 9, from approximately 220 ns onwards the measured signal-to-noise ratio is sufficient to obtain $\langle n_e^{\max} \rangle$ and the radial width σ of the electron density profile as a function of time.

In *phase I*, the increase in $n_e(t)$ is directly related to the upcoming in-band EUV irradiation creating free electrons in the cavity by photoionization of the background gas. Assuming that the majority (~80%) of the gas present is N_2 , the majority of these electrons primarily have an energy (76.4 eV) equal to the difference between the photon energy (92 eV at 13.5 nm) and the ionization potential (15.6 eV for N_2). Note that the electron-energy distribution function (EEDF) is highly non-Maxwellian shortly after the electrons have been produced. In this phase, σ is observed to decrease until the in-band EUV intensity has reached its maximum. At very short timescales (a few ns), the first electrons reach and charge the inner cavity wall while the created ions remain are still fixed in position due to their high inertia. This creates an elevated plasma potential and radially directed electric fields confining additional electrons and preventing them to be lost from the plasma. The observed contraction of the spatial electron distribution is explained by two processes. First, continued production of electrons on the axis of the cavity while its inner surface is already in quasi-equilibrium with the elevated plasma potential results in a spatial electron density distribution which is higher at the axis of the cavity. Second, electrons which have not been involved in charging the inner walls of the cavity start to oscillate through it without reaching the walls. Due to collisions with background molecules, these electrons lose part of their energy. This eventually confines the electron density distribution by the radial electric fields present. For initial electrons with energies in the order of $\varepsilon = 76$ eV, it can be estimated that the collision time of those with the mainly N_2 background gas molecules is indeed in the order of 80-100 ns, as calculated with [45],

$$\tau_{e-N_2}(\varepsilon) = \frac{1}{v(\varepsilon) \sigma_{e-N_2}(\varepsilon) n_{N_2}}, \quad (15)$$

where $v(\varepsilon)$ and $\sigma_{e-N_2}(\varepsilon)$ are the electron velocity and the electron- N_2 collision cross-section respectively, and n_{N_2} is the N_2 density. At the same time, computing the inverse ion plasma frequency by

$$\omega_{pi}^{-1} = \sqrt{\frac{\epsilon_0 m_{N_2^+}}{e^2 n_{N_2^+}}}, \quad (16)$$

yields timescales of the same order (~80 ns). This indicates that, on the same timescales, ions start to move together with the electrons towards the walls, where they eventually recombine.

In *phase II*, the in-band EUV irradiation intensity has passed its maximum value and decreases as a function of time. Consequently, the production of free electrons also decreases while the loss rate due to plasma recombination at the wall continues. Overall, $\langle n_e^{\max} \rangle$ tends to decline over time while the width of this distribution increases due to the expansion of the plasma.

In *phase III*, we observe a special behaviour which has not been seen before. Even though the main in-band EUV irradiation has now faded out, electrons continue to be produced. Since the width of the electron distribution decreases in this phase, these electrons must be produced or gathered along the cavity axis. Although the exact process is not yet fully understood, two processes may be responsible for this behaviour.

First, it is very likely that out-of-band radiation containing photons with energies higher than the ionization threshold of the background gas is responsible for significant photoionization even after the in-band EUV radiation has faded out. As can be seen from the orange curve in figure 9, the shape and timescales of the out-of-band emissions match the observed time evolution of the $\langle n_e^{\max} \rangle$ profile. The fact that a considerable number of electrons is produced even though the out-of-band emission intensity is just a fraction of the in-band one is easily explained by the photoionization cross-section of N_2 , which is more than an order of magnitude higher just above the ionization energy threshold ($2.5 \times 10^{-21} \text{ m}^2$ at 15.6 eV [46]) when compared with its value in the in-band regime ($2.5 \times 10^{-22} \text{ m}^2$ at 92 eV [46]). Second, a significant number of the electrons produced by the in-band radiation (in phases I and II) remain confined in the positive plasma potential during this phase. Whereas the energy loss of 76 eV electrons is initially very fast (<100 ns [45]), electron energy-loss times in 1 Pa N_2 just above ionization thresholds are computed by van de Ven [45] to be $\sim 2 \times 10^2 \mu\text{s}$. Scaling linearly with gas density, this translates to roughly 2 μs for the pressures involved in the experiments reported here.

As during the second part of phase I, the creation of additional electrons on the axis of the cavity combined with cooling of the electron distribution narrows the width of that distribution.

In *phase IV*, production of electrons decreases while the plasma is transported towards the walls, where it decays due to wall recombination.

4.3. Multi-mode MCRS: application for beam power, profile and pointing stability monitor

Output parameters of the multi-mode MCRS measurements are the position ($x_0(t)$, $y_0(t)$) of the maximum $\langle n_e^{\max} \rangle$ of the electron density profile and its width $\sigma(t)$. Once these have been derived from the measurements, absolutely calibrated electron density profiles can be retrieved for every time step. This means that, from an application point of view, the multi-mode MCRS diagnostic presented here can be used as a non-intrusive and in-line beam monitor for ionizing radiation. Parameters that can be derived from this method and used in, say, feedback loops in the source control are: beam power or energy per pulse, cross-sectional beam-intensity profile and pointing stability. This is all due to the fact that the initial electron density profile translates to the cross-sectional shape of the EUV beam and that the number of electrons created translates directly to the EUV pulse energy, i.e. the number of photons (with known photoionization cross-sections, gas

purity and gas pressure). As shown by our measurements, the background gas pressure can be kept low (10^{-4} mbar, or even lower as long as the MCRS signal remains above the lower detection limit) while obtaining sufficient signal for the diagnostics to work.

5. Pulse energy

Traditional MCRS provided cavity-averaged and electric-field-weighted values of the electron density \bar{n}_e . With the development of multi-mode MCRS, the measured electron density is corrected with the distribution of the electric-field component of the resonant mode used. This basically provides—with fixed-cavity geometry—a total number of electrons produced inside the cavity. Knowing the cross-section of the gas used and the instrumental configuration, sufficient data becomes available to determine the time-averaged power or the energy per pulse provided by the source. Of course, the equations used to translate the measured signal into pulse energy depend on the spectral purity filter used, the type of gas and its pressure, and should be determined according to the specific application situation.

6. Beam shape and position

As a demonstration, figure 11 shows the absolutely calibrated and spatially resolved electron density profiles for six different moments in time (denoted with red dashed lines in figure 10) along the x -axis and y -axis of the cavity. Here, we stress again that in the reconstruction procedure (section 2.2.1) a Gaussian profile shape has been used for the radial electron density distribution. This choice was made because in the current application of beam monitoring, one would be mainly interested in the situation at the moment of photoionization by the EUV beam (in which the radial photon density is distributed Gaussian as well). At longer time scales after EUV irradiation, a Bessel-like profile shape may represent plasma dynamics slightly better. Of course, different profile shapes can be used without any problem in the reconstruction method as well. As can be seen from the diagrams in figure 11, both the centre point (x_0 , y_0) and the distribution width σ evolve over time and follow the different phases as explained in the previous section. Additional information that can be retrieved from the plots in figure 11 includes the fact that the EUV-induced plasma is generated (at $t_1 = 0.308 \mu\text{s}$) slightly off the axis of the cavity (i.e. $x_0 = -1.57 \text{ mm}$, $y_0 = -0.76 \text{ mm}$). Furthermore, it can be concluded that—especially in the x -direction—the bulk of the plasma evolves over time in a certain direction. This could be explained by, for example, slight misalignment of the EUV beam with the axis of the cavity or by asymmetrical geometry of or close to the cavity. Another reason might be that the out-of-band EUV-radiation part of the beam is usually wider than its in-band EUV part.

As a direct cross-check for this application, the reconstructed $n_e(x)$ profile at the moment of maximum value of $\langle n_e^{\text{max}} \rangle$ (i.e. at $t_1 = 0.632 \mu\text{s}$) is compared with a fully

independent measurement of the cross-sectional beam-intensity profile (see figure 12). This independent measurement is conducted using an EUV-light-sensitive foil placed at the position of the centre of the cavity and correlates well with the multi-mode MCRS measurements.

7. Conclusions

The following conclusions have been reached from the work presented in this article.

- (1) A novel non-invasive plasma diagnostic called multi-mode microwave cavity resonant spectroscopy (multi-mode MCRS) has been developed and introduced. This is based on traditional MCRS but enables the generation of absolutely calibrated data in a spatially resolved ($100 \mu\text{m}$ resolution) fashion and corrected for the electric-field component of the resonant mode used. It should be noted that this is the first time a diagnostic method has been able to determine spatially resolved distributions of free electrons instantly, and also that its application is not limited to EUV-induced plasmas, as taken as a ‘test case’ here, but also extends to all types of plasmas with electron densities below roughly 10^{17} m^{-3} .
- (2) The electron dynamics during the creation and decay of a highly transient plasma induced by irradiation of a gas at low pressure with a pulsed beam of EUV photons was monitored. Plasma creation and decay were found to match the time evolution of the in-band EUV irradiation, but significant additional production of free electrons was observed at much longer timescales. This behaviour was attributed to production of electrons by photoionization due to ionizing out-of-band radiation from the source and/or by electron-impact ionization by electrons initially created by in-band EUV irradiation.
- (3) The application potential of multi-mode MCRS in monitoring beam properties of ionizing radiation has been demonstrated. The measurements presented in this article show that multi-mode MCRS is able to monitor the pointing stability, cross-sectional intensity profiles and pulse energy of the utilized pulsed beam.

Acknowledgments

The authors acknowledge the financial support of the Dutch funding agency NWO (project number HTSM2015:14651) and of ASML. They are also grateful to the research department of ASML for providing measurement time on its EUV source and to Dr Marco Zangrando from Elettra Sincrotrone Trieste, Italy for fruitful discussions.

Appendix A. CST Microwave Studio simulations of E-field profiles

So-called eigenmode simulations of the electromagnetic resonances in our cavity were performed with CST Microwave

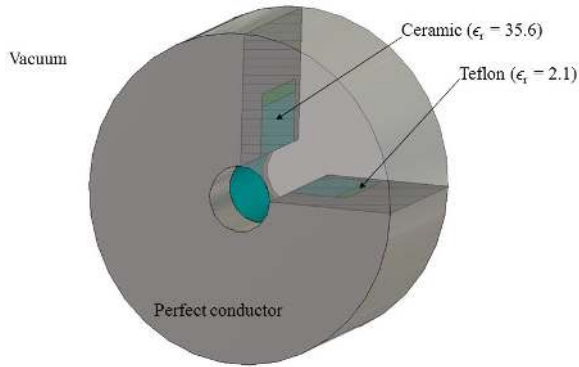


Figure A1. Cut-out of the axisymmetric simulation geometry of the cavity.

Studio. A hexahedral mesh was used in conjunction with the Advanced Krylov Subspace solver. The model geometry is shown in figure A1 and has the same dimensions as the real cavity, though the geometry itself is somewhat simplified (no antenna and associated slots, solid metal housing instead of base plus screw lid). The metals are modelled as perfect electric conductors. The simulation bounding box snugly fits the outside of the cavity, except at the end faces where it extends 10 mm into the vacuum in both directions (z). The total mesh contains a little over 700 000 cells. The ceramic and Teflon were modelled with constant relative permittivities of 35.6 and 2.1 respectively, yielding good correlations between the simulated and measured resonance frequencies of the modes up to 4 GHz. The resulting vectorial electric-field amplitudes within the bounding box, of $-14.5 \text{ mm} \leq x, y \leq 14.5 \text{ mm}$ and $-10 \text{ mm} \leq z \leq 10 \text{ mm}$ (the mass centre of the ceramic is the origin), were interpolated onto a regular rectangular 3D grid with $100 \mu\text{m}$ spacing and exported for processing in Matlab.

Appendix B. Bead-scanning method

Inside the cavity enclosed by the dielectric material, i.e. the volume where the plasma is created, the electric-field component of each resonant mode is determined, spatially resolved, by using a 1.5 mm diameter BaTiO_3 bead connected with superglue to an $80 \mu\text{m}$ thick nylon fishing line to disturb the mode structure locally. By scanning this local disturbance through the volume and monitoring the response of the cavity (in terms of a shift of Δf in the resonance frequency f_0 of the mode under investigation) to it, using Slater’s perturbation theory information about the local electric field $\mathbf{E}(\mathbf{x}_{\text{bead}})$ at the position of a spherical bead \mathbf{x}_{bead} can be retrieved by means of the following equation [39]

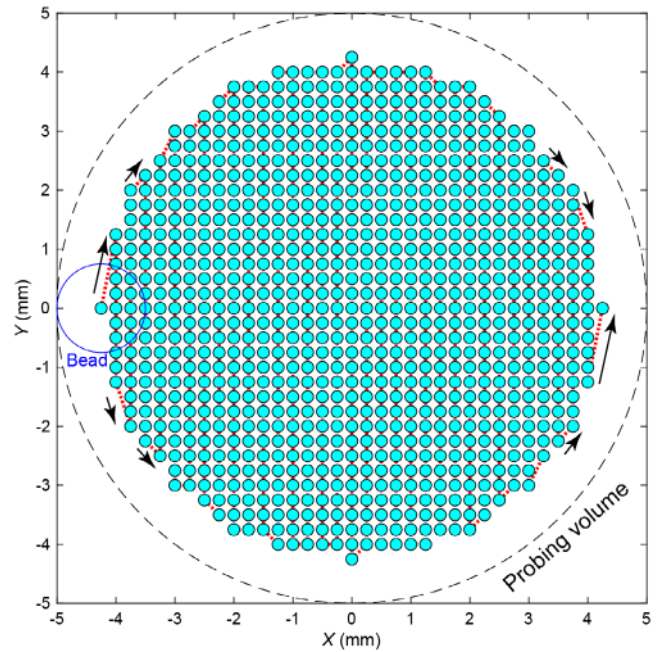


Figure B1. Datapoints, i.e. bead locations, in the XY plane taken into account in the bead-scanning method. The arrows indicate the trajectory the bead followed over time. For each relevant resonant mode, the cavity response $\Delta f/f_0$ has been measured for each of these datapoints; this procedure has been repeated for 41 Z positions along the axis of the cavity.

$$\frac{\Delta f}{f_0} \cong \frac{3 \epsilon_r - 1}{2 \epsilon_r + 2} \frac{\int \int \int_{\text{bead}} |\mathbf{E}(\mathbf{x})|^2 d^3 \mathbf{x}}{\int \int \int_{\text{cav}} |\mathbf{E}(\mathbf{x})|^2 d^3 \mathbf{x}} \approx \frac{3 \epsilon_r - 1}{2 \epsilon_r + 2} \frac{V_{\text{bead}} |\mathbf{E}(\mathbf{x})|^2}{\int \int \int_{\text{cav}} |\mathbf{E}(\mathbf{x})|^2 d^3 \mathbf{x}}. \quad (\text{B.1})$$

This shows that $|\mathbf{E}(\mathbf{x}_{\text{bead}})|^2 \propto \frac{\Delta f}{f_0}$. In practice, in the bead-scanning method, $\frac{\Delta f}{f_0}$ is measured for each relevant resonant mode and for fixed positions \mathbf{x}_{bead} of the bead. During the calibration measurements, the bead was directed through the volume by an automated XYZ translation stage with spatial resolutions of $250 \mu\text{m}$ in both the X and Y planes (see figure B1) and of $500 \mu\text{m}$ in the Z plane. The holes in the top and bottom lids of the cavity—serving as the entrance and exit for the EUV radiation—might be responsible for ‘leakage’ of part of the mode structure outside the cavity. To be able to take this effect into account and to correct for it during absolute calibration, the electric field distribution is scanned in the Z direction from 2.5 mm below the bottom lid of the cavity up to 2.5 mm above its top lid. In all, a spatially resolved measurement of the electric field profile for each single resonant mode consists of 36941 datapoints.

Appendix C. Additional results from bead-scanning and CST microwave studio simulations

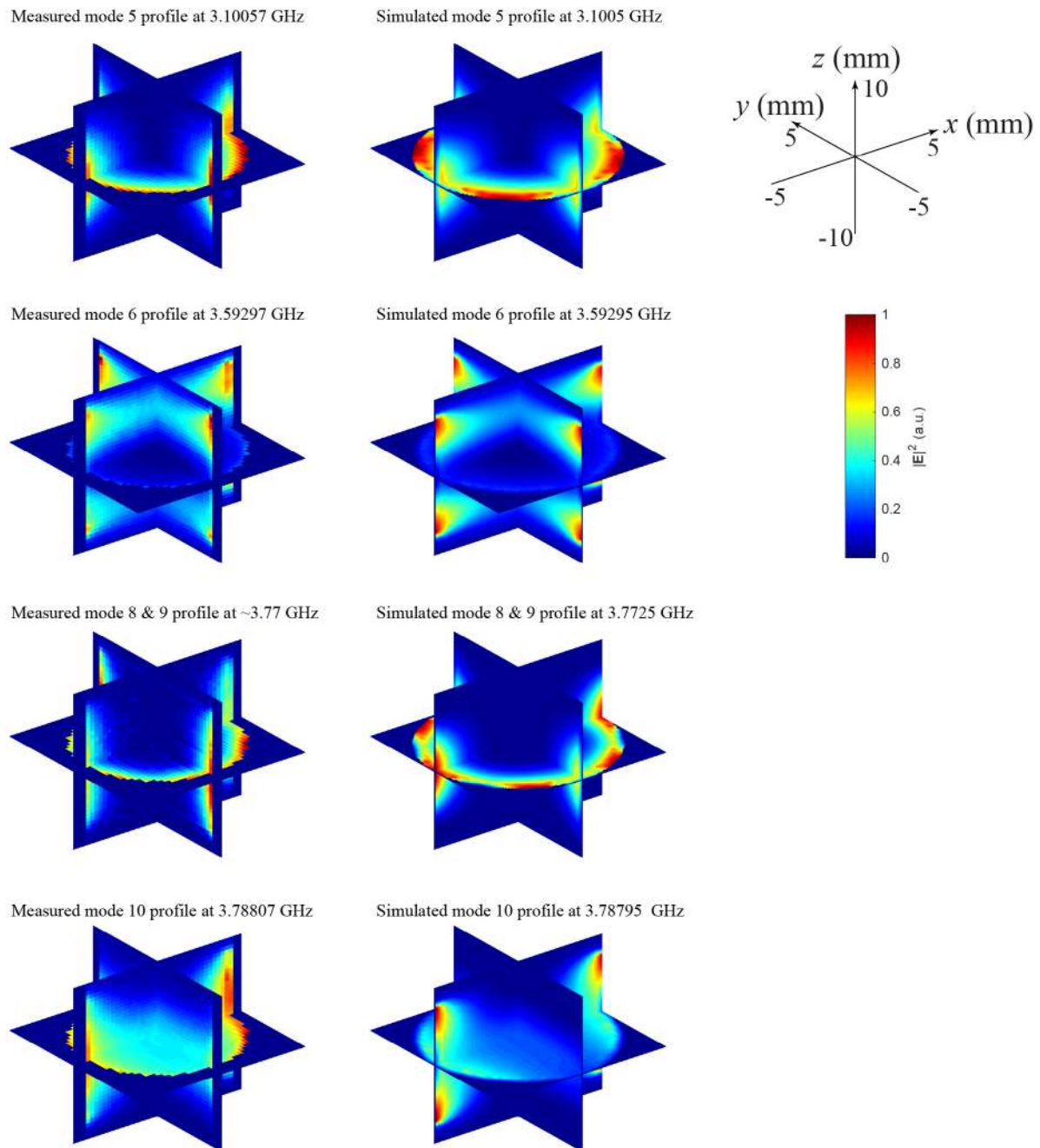


Figure C1. Electric-field profiles obtained experimentally using the bead-scanning method (left column) and simulated using the CST Microwave Studio package (right column) for modes 5, 6, 8, 9 and 10.

ORCID iDs

J Beckers  <https://orcid.org/0000-0001-6116-7013>

References

- [1] Born M and Wolf E 1980 *Principles of Optics* (Oxford: Pergamon)
- [2] Benschop J, Banine V, Lok S and Loopstra E 2008 Extreme ultraviolet lithography: status and prospects *J. Vac. Sci. Technol. B* **26** 2204–7
- [3] van der Velden M H L, Brok W J M, van der Mullen J J A M and Banine V Y 2006 Kinetic simulation of an extreme ultraviolet radiation driven plasma near a multilayer mirror *J. Appl. Phys.* **100** 73303
- [4] Dolgov A *et al* 2014 Comparison of H₂ and He carbon cleaning mechanisms in extreme ultraviolet induced and surface wave discharge plasmas *J. Phys. D: Appl. Phys.* **47** 65205
- [5] Nishiyama Y *et al* 2008 Carbon contamination of EUV mask: film characterization, impact on lithographic performance, and cleaning *Emerging Lithographic Technologies XII, PTS 1 and 2* vol 6921
- [6] Hopf C, von Keudell A and Jacob W 2003 Chemical sputtering of hydrocarbon films *J. Appl. Phys.* **94** 2373–80
- [7] Chen J *et al* 2011 Carbon-induced extreme ultraviolet reflectance loss characterized using visible-light ellipsometry *Meas. Sci. Technol.* **22** 114026

- [8] Bondareva A L and Zmievskaya G I 2010 Computer simulation of blistering in multilayer mirrors for EUV lithography *J. Surf. Investig. X-ray Synchrotron Neutron Tech.* **4** 480–7
- [9] van den Bos R A J M, Lee C J, Benschop J P H and Bijkerk F 2017 Blister formation in Mo/Si multilayered structures induced by hydrogen ions *J. Phys. D: Appl. Phys.* **50** 265302
- [10] Kuznetsov A S, Gleeson M A and Bijkerk F 2013 Ion effects in hydrogen-induced blistering of Mo/Si multilayers *J. Appl. Phys.* **114** 113507
- [11] Kuznetsov A S, Kruijs R W E, Gleeson M A, Schmid K and Bijkerk F 2010 Hydrogen interaction with EUVL-relevant optical materials *J. Surf. Investig. X-ray Synchrotron Neutron Tech.* **4** 563–6
- [12] Abrikosov A et al 2017 Numerical simulations based on probe measurements in EUV-induced hydrogen plasma *Plasma Sources Sci. Technol.* **26** 45011
- [13] Astakhov D I et al 2016 Exploring the electron density in plasma induced by EUV radiation: II. Numerical studies in argon and hydrogen *J. Phys. D: Appl. Phys.* **49** 295204
- [14] van Der Horst R M, Beckers J, Nijdam S and Kroesen G M W 2014 Exploring the temporally resolved electron density evolution in extreme ultra-violet induced plasmas *J. Phys. D: Appl. Phys.* **47** 302001
- [15] van Der Horst R M, Osorio E A, Banine V Y and Beckers J 2016 The influence of the EUV spectrum on plasma induced by EUV radiation in argon and hydrogen gas *Plasma Sources Sci. Technol.* **25** 015012
- [16] van Der Horst R M, Beckers J, Osorio E A and Banine V Y 2015 Dynamics of the spatial electron density distribution of EUV-induced plasmas *J. Phys. D: Appl. Phys.* **48** 065016
- [17] van Der Horst R M, Beckers J, Osorio E A and Banine V Y 2015 Exploring the electron density in plasmas induced by extreme ultraviolet radiation in argon *J. Phys. D: Appl. Phys.* **48** 285203
- [18] van Der Horst R M et al 2016 Exploring the electron density in plasma induced by EUV radiation: I. Experimental study in hydrogen *J. Phys. D: Appl. Phys.* **49** 145203
- [19] Beckers J, van Der Horst R M, Osorio E A, Kroesen G M W and Banine V Y 2016 Thermalization of electrons in decaying extreme ultraviolet photons induced low pressure argon plasma *Plasma Sources Sci. Technol.* **25** 035010
- [20] van De Ven T H M, De Meijere C A, van Der Horst R M, van Kampen M, Banine V Y and Beckers J 2018 Analysis of retarding field energy analyzer transmission by simulation of ion trajectories *Rev. Sci. Instrum.* **89** 043501
- [21] van De Ven T H M et al 2018 Ion energy distributions in highly transient EUV induced plasma in hydrogen *J. Appl. Phys.* **123** 063301
- [22] Carbone E and Nijdam S 2015 Thomson scattering on non-equilibrium low density plasmas: principles, practice and challenges *Plasma Phys. Control. Fusion* **57** 014026
- [23] van der Velden M 2008 *Radiation Generated Plasmas: A Challenge in Modern Lithography* (Eindhoven: University of Technology Eindhoven)
- [24] Brown S C and Rose D J 1952 Methods of measuring the properties of ionized gases at high frequencies. I. Measurements of Q *J. Appl. Phys.* **23** 711–8
- [25] Rose D J and Brown S C 1952 Methods of measuring the properties of ionized gases at high frequencies. II. Measurement of electric field *J. Appl. Phys.* **23** 719–22
- [26] Rose D J and Brown S C 1952 Methods of measuring the properties of ionized gases at high frequencies. III. Measurement of discharge admittance and electron density *J. Appl. Phys.* **23** 1028–32
- [27] Haverlag M, Kroesen G M W, Bisschops T H J and DeHoog F J 1991 Measurement of electron-densities by a microwave cavity method 13.56 MHz RF plasmas of AR, CF₄, C₂F₆, and CHF₃ *Plasma Chem. Plasma Process.* **11** 357–70
- [28] Stoffels E, Stoffels W W, Vender D, Kando M, Kroesen G M W and DeHoog F J 1995 Negative ions in a radio-frequency oxygen plasmas *Phys. Rev. E* **51** 2425–35
- [29] Stoffels E and Stoffels W W 1994 Electrons, ions and dust in a radio-frequency discharge *PhD Thesis* Eindhoven University Technology
- [30] Vender D, Stoffels W W, Stoffels E, Kroesen G M W and DeHoog F J 1995 Charged-species profiles in electronegative radiofrequency plasmas *Phys. Rev. E* **51** 2436–44
- [31] Stoffels W W, Sorokin M and Remy J 2008 Charge and charging of nanoparticles in a SiH₄ rf-plasma *Faraday Discuss.* **137** 115–26
- [32] van De Wetering F M J H, Beckers J and Kroesen G M W 2012 Anion dynamics in the first 10 milliseconds of an argon-acetylene radio-frequency plasma *J. Phys. D: Appl. Phys.* **45** 485205
- [33] van De Wetering F M J H, Brooimans R J C, Nijdam S, Beckers J and Kroesen G M W 2015 Fast and interrupted expansion in cyclic void growth in dusty plasma *J. Phys. D: Appl. Phys.* **48** 035204
- [34] Beckers J, Stoffels W W and Kroesen G M W 2009 Temperature dependence of nucleation and growth of nanoparticles in low pressure Ar/CH₄ RF discharges *J. Phys. D: Appl. Phys.* **42** 155206
- [35] van Der Horst R M, Beckers J, Osorio E A, van De Ven T H M and Banine V Y 2015 Radiating plasma species density distribution in EUV-induced plasma in argon: a spatiotemporal experimental study *Plasma Sources Sci. Technol.* **24** 065016
- [36] Lieberman M A and Lichtenberg A J 2005 *Principles of Plasma Discharges and Materials Processing* 2nd edn (New York: Wiley)
- [37] van der Horst R M 2005 *Electron Dynamics in EUV-Induced Plasmas* (Eindhoven: Eindhoven University of Technology)
- [38] Zocchi E and Benedetti F E 2007 Optical designs of grazing incidence collector for extreme ultraviolet lithography *J. Micro/Nanolithogr. MEMS MOEMS* **6** 043002
- [39] Lassise A C 2012 *Miniaturized RF Technology for Femtosecond Electron Microscopy* (Eindhoven: Eindhoven University of Technology)
- [40] Lassise A, Mutsaers P H A and Luiten O J 2012 Compact, low power radio frequency cavity for femtosecond electron microscopy *Rev. Sci. Instrum.* **83** 43705
- [41] van De Wetering F M J H, Nijdam S and Beckers J 2016 Conclusive evidence of abrupt coagulation inside the void during cyclic nanoparticle formation in reactive plasma *Appl. Phys. Lett.* **109** 043105
- [42] van de Wetering F M J H 2016 *Formation and Dynamics of Nanoparticles in Plasmas* (Eindhoven: Eindhoven University of Technology)
- [43] Maier L C and Slater J C 1952 Field strength measurements in resonant cavities *J. Appl. Phys.* **23** 68–77
- [44] Banine V Y, Brussaard G J H, Koppert W J C, Luiten O J, Nienhuys H, Beckers J and van der Horst R M 2016 Radiation sensor apparatus WO2016139022A1 *US Patent Specification* US20180058928A1
- [45] van de Ven T H M 2018 *Ion Fluxes Towards Surfaces Exposed to EUV-Induced Plasmas* (Eindhoven: Eindhoven University of Technology)
- [46] Samson G C, Masuoka J A R, Pareek T and Angel P N 1987 Total and dissociative photoionization cross sections of N₂ from threshold to 107 eV *J. Chem. Phys.* **86** 6128
- [47] Adam Lassise A 2018 internal communication